

# Nonlinearity of Degenerately Doped Bulk-Mode Silicon MEMS Resonators

Yushi Yang, Eldwin J. Ng, Pavel M. Polunin, Yunhan Chen, Ian B. Flader, Steven W. Shaw, Mark I. Dykman, and Thomas W. Kenny

**Abstract**—We present an experimental study of conservative nonlinearities in bulk acoustic mode (bulk-mode) silicon MEMS resonators with degenerate doping. Three types of bulk acoustic mode resonators oriented in  $\langle 110 \rangle$  and  $\langle 100 \rangle$  silicon crystalline directions are used to analyze both linear and nonlinear elastic behavior of silicon with p- ( $N \cong 4.19e + 18$  to  $1.63e + 20 \text{ cm}^{-3}$ ) and n-type ( $N \cong 1.58e + 18$  to  $5.91e + 19 \text{ cm}^{-3}$ ) doping. For accurate characterization of the amplitude-dependent nonlinear stiffness constant, we employ two methods: amplitude-frequency response and ringdown measurement. Experimental results show that the nonlinear behavior of these resonators is dominated by material-dependent mechanical nonlinearities and strongly depends on the doping type and crystal orientation. These results are useful for understanding the material-induced nonlinear properties of doped silicon and design of MEMS resonators with desired dynamic behavior, and may provide a new avenue for tailoring resonator response characteristics. [2015-0301]

**Index Terms**—Bulk acoustic mode resonators, material nonlinearity, degenerate doping.

## I. INTRODUCTION

CAPACITIVE microelectromechanical (MEMS) oscillators represent a promising alternative to quartz-based systems as they provide benefits such as mass fabrication, size reduction, and compatibility with CMOS IC integration [1], [2]. Commercial viability has been achieved by relying on established integrated circuit fabrication processes and reliable wafer-scale packaging techniques [3], [4]. However, one drawback that comes with size reduction is smaller capacitances and smaller induced currents, which can lead to increased noise in the oscillator output. To overcome this

Manuscript received November 12, 2015; revised April 28, 2016; accepted June 23, 2016. Date of publication July 15, 2016; date of current version September 29, 2016. This work was supported in part by the Defense Advanced Research Projects Agency through the Mesodynamic Architectures Program managed by Dr. J. Rogers and Dr. D. Green under Grant FA8650-13-1-7301, and in part by the Stanford Nanofabrication Facility within the National Science Foundation through the National Nanotechnology Infrastructure Network for Fabrication Work under Grant ECS-9731293. This is a collaboration work between Stanford University and Michigan State University. Subject Editor R. Pratap.

Y. Yang, E. J. Ng, Y. Chen, I. B. Flader, and T. W. Kenny are with the Mechanical Engineering Department, Stanford University, Stanford, CA 94305 USA (e-mail: yushiyang@mems.stanford.edu; eldwin@mems.stanford.edu; yunhanc@mems.stanford.edu; iflader@mems.stanford.edu; tkenny@stanford.edu).

P. M. Polunin and S. W. Shaw are with the Mechanical Engineering Department, Michigan State University, East Lansing, MI 48824 USA (e-mail: poluninp@msu.edu; shawsw@msu.edu).

M. I. Dykman is with the Physics and Astronomy Department, Michigan State University, East Lansing, MI 48824 USA (e-mail: dykman@pa.msu.edu).

Color versions of one or more of the figures in this paper are available online at <http://ieeexplore.ieee.org>.

Digital Object Identifier 10.1109/JMEMS.2016.2586099

challenge, resonators have to be driven to larger amplitudes of motion in order to maintain high signal-to-noise ratio, and oftentimes this requires operating resonators in the nonlinear regime [5], [6]. In this regime the resonator dynamics can become much more complicated due to nonlinear effects such as amplitude-dependent frequency shift [7] and nonlinear dissipation [8], [9].

Conservative nonlinearities in capacitive MEMS resonators can be categorized into electrostatic and mechanical nonlinearities. Mechanical nonlinearities can further be subdivided as originating from kinematics (e.g. mid-plane stretching of Euler-Bernoulli beam [10], [11]) and intrinsic material effects. While geometric and electrostatic effects frequently dominate the dynamics of flexural modes [12], in bulk-mode resonators the material nonlinear elastic effects often play a major role [13]–[15]. Since bulk-mode resonators can offer quality factors ( $Q$ ) and energy storage that are orders-of-magnitude higher than flexural resonators, they are hence more desirable for high performance frequency/timing references [5], [13]–[15], and are the focus of this work.

Doping processes are commonly used in MEMS fabrication as means of creating electrically conductive layers for transducers, heaters, and other MEMS structures. Recent research has also demonstrated the use of heavily p- or n-type doping for passive frequency-temperature compensation [16]–[18]. Introducing dopants to the silicon lattice are known to shift the semiconductor energy bands, resulting in a change in the material elastic constants [19], [20]. Because of the potential for significant reduction of the frequency-temperature coefficients for MEMS resonators and a variety of micromechanical sensors, it is important to understand the material properties of degenerately-doped silicon.

Previous research has demonstrated the nonlinear limits of bulk-mode resonators, but not many detailed analyses have been done on the effect of doping on nonlinearity. Kaajakari *et al.* have developed an analytical model for the nonlinear engineering Young's modulus, which incorporates both geometrical and material effects for a longitudinal mode beam resonator. However, the discrepancy between experimental and analytical results is around 40%, which arises from their use of elastic constants for undoped silicon rather than that of doped silicon in the analytical calculation [13]. Zhu *et al.* analyzed the material nonlinearity limit of a Lamé mode resonator, and reported opposite nonlinear behaviors for devices oriented in  $\langle 110 \rangle$  and  $\langle 100 \rangle$  crystalline directions [15]. Wang *et al.* [21] and Bijari *et al.* [22] studied the nonlinear effect of bulk-mode ring resonators and showed

that material nonlinearity plays an important role in the system's nonlinear behavior. Shahmohammadi *et al.* reported that nonlinearity in n-type doped silicon resonators can be reduced by possibly modifying the doping concentration and resonator alignment to a different crystalline orientation [23].

This manuscript builds on the work presented in [24], where the nonlinear elasticity of silicon was observed to be strongly dependent on doping. We aim to characterize the nonlinearities in bulk-mode silicon MEMS resonators using conventional spectral methods (i.e. frequency response) and ringdown measurements. The rest of the paper is organized as follows: in §II, we present a phenomenological model for nonlinear oscillations and describe two ways of characterizing the system: amplitude-frequency response and time-domain analysis. Section III provides a brief summary of the sources of nonlinearities in capacitive microresonators. Section IV summarizes the resonators characteristics used in this study, where the resonator design, fabrication method, and measurement setup are listed in detail. Experimental results for using both the frequency-response analysis and ringdown measurement are documented in §V, and discussions are made in §VI. Lastly, concluding remarks are made in §VII.

## II. MODELING NONLINEAR OSCILLATIONS

To study the dynamics of a vibrational mode in a nonlinear MEMS resonator, we represent it by a single degree-of-freedom lumped mass system and describe its forced response by the equation of motion:

$$m\ddot{x} + c\dot{x} + k_0x + k_1x^2 + k_2x^3 = F\cos(\omega t), \quad (1)$$

where  $x$  is the modal displacement,  $m$  is the effective mass,  $c$  is the linear damping coefficient,  $k_0$  is the linear spring constant,  $k_1$  and  $k_2$  represents the nonlinear spring constants, and  $F$  is the magnitude of the external periodic driving. We also define the modal natural frequency as  $\omega_0 = \sqrt{k_0/m}$  and linear quality factor as  $Q = \omega_0 m/c$ .

For capacitive microresonators, the spring constants include contributions from both mechanical ( $k_m$ ) and electrical ( $k_e$ ) restoring forces (see §III). While various methods can be used to analyze the dynamics of MEMS resonators [25], in this paper we utilize two techniques to study the nonlinear behavior of the vibrational modes: spectral (“frequency response”) and time-domain (“ringdown”) measurements.

### A. Analysis of Frequency Response

In this work we exploit the analytical results of (1) given in [26] and [27], where in the presence of stiffness nonlinearity, the resonant frequency ( $f$ ) changes as a function of the resonance amplitude ( $a$ )

$$f \cong f_0 + \kappa a^2 \rightarrow \kappa = \Delta f/a^2, \quad (2)$$

where  $\kappa$  is commonly known as the amplitude-frequency coefficient ( $A$ - $f$  coefficient), and can be estimated by the anharmonic stiffness coefficients [26], [27]:

$$\kappa = \left( \frac{3}{8} \frac{k_2}{k_0} - \frac{5}{12} \frac{k_1^2}{k_0^2} \right) f_0. \quad (3)$$

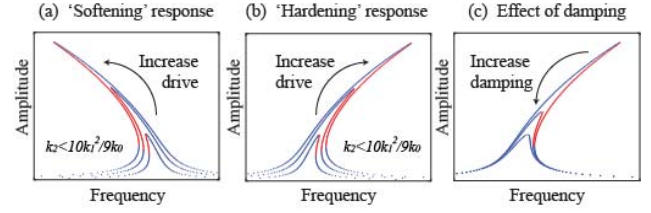


Fig. 1. Simulated frequency response of (a) softening response, (b) hardening response, and (c) effect of damping on the nonlinear behavior. The red curve represents unstable branches of the solution, while the blue curves represent the stable branches.

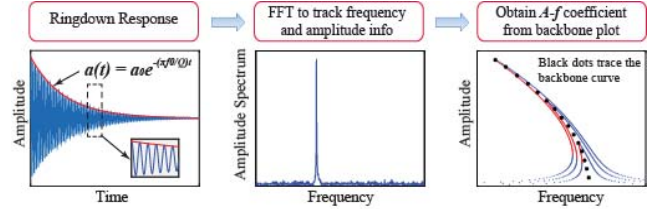


Fig. 2. Extracting the  $A$ - $f$  coefficient  $\kappa$  from ringdown measurements. The ringdown data is first divided into multiple bins and an FFT is performed on each bin to extract the frequency and amplitude information.  $\kappa$  can be extracted by fitting the amplitude-frequency relation with the backbone parabola.

Depending on the relative strength of  $k_0$ ,  $k_1$  and  $k_2$ , the system can exhibit either “softening” or “hardening” responses (Fig. 1a - 1b). The damping coefficient  $c$  affects the resonator dynamics by imposing a limit on the resonance amplitude

$$a_{peck} = \frac{F}{c\omega_0} = \frac{FQ}{\omega_0^2 m}. \quad (4)$$

Equation (4) indicates that the interplay of the external driving amplitude and the resonator dissipation rate plays an important role on whether or not the resonator operates in its nonlinear regime for a given value of Duffing constant (Fig.1c).

### B. Analysis of Ringdown Response

A standardized way to obtain a ringdown response is by imposing a periodic drive near the resonant frequency of the mode of interest, so that the system response is dominated by that mode, and then turning off the external drive, resulting in a decaying transient vibration. By sampling the waveform at a rate that is much faster than the resonant frequency, it is possible to capture a detailed picture of the resonator ringdown, estimate the value of  $Q$ , and establish the relationship between the vibrational amplitude and frequency throughout the decay.

Information about the vibrational frequency during the ringdown can be extracted in several ways. In this work, we divide the whole response into multiple bins and perform a Fast Fourier Transform (FFT) on each bin to obtain the time-varying frequency and amplitude spectrum (Fig. 2). Subsequent interpolation of the frequency spectrum can be used to improve the estimation of the frequency at each bin. The benefit of this FFT method compared to other ringdown

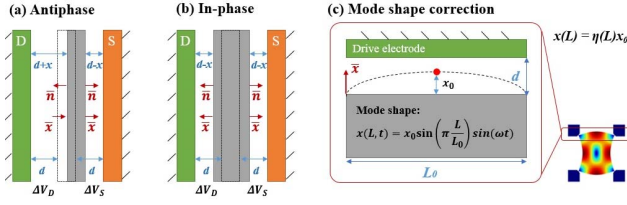


Fig. 3. (a) Antiphase, and (b) in-phase configuration. Depending on the electrode configuration, electrostatic forcing and spring constants needs to be calculated differently. (c) Example of mode shape correction for a Lamé mode resonator. Note that depending on the operation mode shape and surface outward normal,  $\eta$  can be either positive or negative.

fitting methods, such as raw data equation fitting or envelope detection, are that: 1) out-of-band noise and higher order harmonics are effectively eliminated for accurate measurement of the desired fundamental frequency signal; 2) precise estimation of the fundamental frequency can be performed (ppm-level accuracy for these high frequency resonators); 3) the algorithm is typically much faster than raw data fitting for high frequency/high  $Q$  devices with numerous data points (typically about 100 million points).

Unlike the forced vibrations described by (1), the ringdown response represents the resonator free motion (i.e.  $F = 0$ ). As a result of the amplitude decay, the ringdown vibrational frequency, being dependent on the amplitude, also changes in time and follows the so-called backbone curve – the frequency response of unforced and undamped oscillator [9]. This backbone curve tracks the locus of the maximal oscillation amplitudes (for high  $Q$  device) as the excitation level increases and can be represented as a polynomial function of the amplitude in (2). It is worth mentioning that a combination of electrostatic, material, and mechanical nonlinearities can result in backbone curves that change from hardening to softening as a function of amplitude [12], [28]. In this work, we will focus on analyzing nonlinear stiffness terms up to the 3<sup>rd</sup> order.

### III. NONLINEARITIES IN CAPACITIVE MICRORESONATORS

Conservative nonlinearities in electrostatically-actuated resonators can be separated into intrinsic mechanical nonlinearities and nonlinearities associated with electrostatic excitation. Generally, mechanical nonlinearities arise due to large strain when approximations for linear elasticity do not hold, and is strongly depend on the material and the resonator geometry. In contrast, electrostatic nonlinearities are generally caused by the variable gap capacitive transduction, and is determined by the geometry and configuration of both the resonator and electrodes (Fig. 3a-3b). As a result, these two groups of nonlinearities can reveal themselves at different vibrational amplitudes.

#### A. Electrostatic Nonlinearity

The effective electrostatic excitation force  $f$  in (1) can be reduced to a 1D lumped-mass model as:

$$F = \frac{dU_e}{dx}, \quad (5)$$

$$U_e = \frac{h}{2} \epsilon_0 (V_b - V_{ac})^2 \sum_i^N \int_{L_i} \left( \frac{1}{d_0 - \bar{n} \cdot \bar{x}(L)} \right) dL, \quad (6)$$

where the subscript  $i$  denotes individual electrodes,  $N$  is the total number of electrodes,  $U_e$  represents the electrostatic energy between the electrode and resonator body,  $\bar{x}(L)$  is the resonator displacement profile along the electrode,  $\bar{n}$  is the outward normal unit vector of each electrode surface,  $h$  is the resonator thickness,  $d_0$  is the initial gap size,  $V_b$  and  $V_{ac}$  represent the dc bias voltage and ac excitation voltage respectively, and  $\epsilon_0$  is the cavity permittivity, which is believed to be near-vacuum for these devices [27]. Considering the non-uniform displacement profiles associated with different mode shape (Fig. 3c), a mode shape correction factor  $\eta$  is introduced as

$$\bar{n} \cdot \bar{x}(L) = \eta x_0, \quad (7)$$

where  $x_0$  is the resonator's maximum displacement. The electrical spring constants with respect to  $x_0$  can be found by performing Taylor expansion to (6), and combining (5) - (7), where the final result is estimated as:

$$k_e \cong -\frac{h}{2} \epsilon_0 V_b^2 \sum_i^N \int_{L_i} \left( \frac{2}{d_0^3} \eta_i^2 + \frac{3}{d_0^4} \eta_i^3 x_0 + \frac{4}{d_0^5} \eta_i^4 x_0^2 \right) dL. \quad (8)$$

The negative sign in front of the spring constants indicates that electrostatic actuation reduces the effective stiffness coefficients. As a result, the 1<sup>st</sup> order electrostatic spring constant ( $k_{0e}$ ) shifts the resonant natural frequency as a function of bias voltage:

$$f_0 = \frac{1}{2\pi} \sqrt{\frac{1}{m} (k_{0m} + k_{0e})} \cong \frac{1}{2\pi} \sqrt{\frac{1}{m} \left( k_{0m} - \frac{N \epsilon_0 V_b^2 A}{d_0^3} \right)}, \quad (9)$$

Equation (9) is known as the electrostatic frequency tuning effect. The higher order electrostatic spring coefficients (i.e.  $k_{1e}$  and  $k_{2e}$ ) reduce the nonlinear resonant frequency and cause the modal frequency response to bend towards lower frequency as displacement increases (Fig. 1a).

#### B. Mechanical Nonlinearity


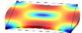

Mechanical nonlinearities arise due to intrinsic properties of the crystal lattice (material nonlinearities) and/or when accounting for additional kinematic effects (geometric nonlinearities). Material nonlinear effects are generally attributed to the nonlinear stress-strain relationship within the resonator body under large deformations:

$$E = E_0 + E_1 \epsilon + E_2 \epsilon^2, \quad (10)$$

where  $\epsilon$  is the engineering strain,  $E_0$  is the linear Young's modulus,  $E_1$  and  $E_2$  are higher order corrections due to large strain. The material nonlinearity for degenerately-doped silicon strongly depends on the interaction between the energy bands and the strains [20]. These interactions can be highly-complex, and have not been completely modeled. Since different resonators have different operating mode shapes, the stress-strain distribution for a specific operating mode has to be taken into consideration to accurately model nonlinear vibration. For commonly used bulk-mode resonators,



TABLE I  
LIST OF RESONATOR PARAMETERS

Parameter and Symbol	LE	Lamé	Ring
Mode shape			
Length ( $L_0$ ), $\mu\text{m}$	600	400	N/A
Width ( $W_0$ ), $\mu\text{m}$	300	400	N/A
Inner radius ( $R_m$ ), $\mu\text{m}$	N/A	N/A	59
Outer radius ( $R_n$ ), $\mu\text{m}$	N/A	N/A	69
Height ( $h$ ), $\mu\text{m}$	20	20	40
Gap ( $d_0$ ), $\mu\text{m}$	$1.2 \pm 0.2$	$1.1 \pm 0.2$	$1.6 \pm 0.2$
Effective mass ( $m$ ), $\mu\text{g}$	4.15	3.73	0.50
Frequency ( $f_0$ ), MHz	<110>	$7 \pm 0.2$	$10 \pm 0.2$
	<100>	$6 \pm 0.2$	$8 \pm 0.2$
Quality factor ( $Q$ )	1.1 – 1.5 M	1.3 – 2 M	250 – 300 k

\* Note:  $d_0$ ,  $f_0$ , and  $Q$  varies slightly between devices. The listed values are the range for all device tested.

the equations of motion incorporating nonlinear Young's moduli have been developed in [7], [15], and [21] and are summarized in Appendix. In this paper, we will focus on analyzing the system response and characterizing how doping affects the  $A$ - $f$  coefficient.

As for geometric nonlinearities, the assumptions of infinitesimal strains and small rotations in Euler-Bernoulli theory remain valid as long as the resonator vibration amplitudes are moderately small. When the displacement of the resonator body becomes comparable with a typical length scale of the system, geometric nonlinearities cannot be neglected. While this effect can be significant in flexural mode resonators, the most commonly seen geometric nonlinearities in bulk-mode resonators are caused by Poisson induced volume changes at large deformations [13], [21], [20]. Since material and geometric nonlinearities appear in the modal dynamics due to two different mechanisms, they both may be present in any particular resonator.

#### IV. RESONATOR CHARACTERIZATIONS

##### A. Resonator Design

Three types of bulk-mode resonators are used in this study: length extensional modes (LE), Lamé modes (Lamé), and dual breathe-mode ring resonators (Ring). The simulated mode shapes and design parameters are listed in Table I.

It is worth noting that some resonator parameters can be obtained with finite element simulation prior to the device characterization. First, the effective mass of the resonators can be estimated using (11), where the resonator displacement field  $u$  across the mode shape is first normalized with respect to the resonator's maximum displacement  $x_0$ , followed by an integration across the entire volume

$$m = \iiint_{Vol} \rho \left( \frac{u}{x_0} \right)^2 dV, \quad (11)$$

where  $\rho$  is the density of silicon ( $2330 \text{ kg/m}^3$ ). The simulated effective mass will be used in later analysis to facilitate parameter extraction from the electrostatic frequency tuning measurement (see §V-A). Additionally, the linear mechanical spring constant can also be estimated. Previous research has

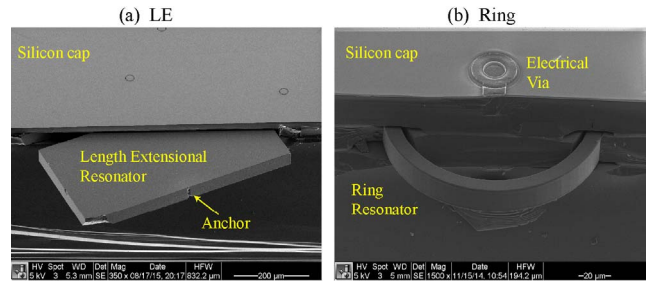


Fig. 4. SEM of (a) LE resonator without release etch holes in the device layer, and (b) ring resonator.

shown that doping will affect the 2<sup>nd</sup> order elastic tensor of silicon [17], [18], which implies that the linear mechanical spring constant should be modified accordingly. Using values of the elastic constants for doped silicon in [17] and interpolating these data to account for the doping level used in this work, we can obtain the linear mechanical spring constants (see [30] for list of mechanical spring constants).

##### B. Fabrication

The resonators used in this study were fabricated using a wafer-level epitaxial encapsulation process (*epi-seal*). The *epi-seal* process is a hermetic encapsulation process which provides a low-pressure (sub-Pascal), ultra-clean operating environment free of native oxide [31]. The baseline process was developed by researchers at Stanford University and Bosch RTC in Palo Alto. Resonators fabricated in this process have demonstrated high performance characteristics such as ppb-level stability [29] and high  $Q$  [32], thus making it an excellent platform for this study. However, one design limitation of the baseline process is the requirement of release etch-holes, which has shown to severely decrease the resonator  $Q$  [33]. As seen in (4), a high damping coefficient will suppress the nonlinear effect, therefore to study the nonlinearity limit of these bulk-mode devices, high  $Q$  is desired.

In this work, the Ring resonators with  $Q$ s of around 250k were fabricated using the baseline *epi-seal* process detailed in [29], while the LE and Lamé resonators were fabricated in a modified process [34] with measured  $Q$ s all exceeding 1 M. The modified process preserves the benefits of the *epi-seal* process while adding the capability of fabricating bulk-mode resonators without release etch-holes (see Fig. 4), thus decreasing the thermoelastic dissipation. The wafer dopant types and doping levels used in this study are listed in Table II. The resistivity is obtained by performing a 5-point measurement using a Prometrix RS35e Resistivity Mapping System prior to device fabrication, and the resistivity-to-mobility conversion is done using [35].

##### C. Measurement Setup

The experimental setup is shown in Fig. 5. The encapsulated devices were first wire-bonded to a package, mounted on a printed circuit board, and then placed into a Thermotron S-1.2c environmental chamber for temperature control. For all the experiments performed, the temperature was held constant at 0°C. A Zurich HF2LI lock-in amplifier was used

TABLE II  
 DOPANT TYPE AND DOPING LEVEL

Wafer	Dopant	Resistivity, mΩ-cm	Concentration, cm <sup>-3</sup>
PBH	Boron	1.4	8.7e+19
		Lamé: 0.8 Ring: 0.9	Lamé: 1.6e+20 Ring: 1.5e+20
PBL	Boron	16.4, Ring: 15.9	4.2e+18 Ring: 4.4e+18
NPH	Phosphorous	1.3 Ring: 1.8	5.9e+19 Ring: 4.1e+19
NAM	Arsenic	3.5 Ring: 3.1	2.0e+19 Ring: 2.4e+19
NSL	Antimony	11.7	2.8e+18
		Ring: 17.1	Ring: 1.6e+18

\* The resistivities and concentrations are the same for all devices unless noted otherwise. The wafer labeling follows the logic: doping type, dopant, and level of doping (H: high; M: medium; L: low).

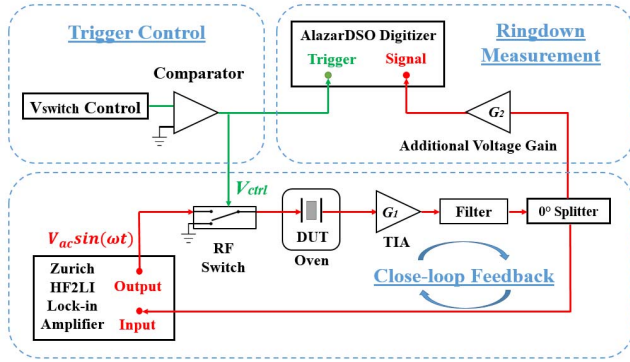


Fig. 5. Experimental setup used in this study.

to maintain a variable-phase feedback loop. The ac output from the lock-in amplifier was used to excite the resonator, while the resonator body was biased with a dc voltage. The resonator's output current was converted to a voltage signal and amplified via a trans-impedance amplifier (TIA). After passing through a band-pass filter, the signal was split into two outputs with a 0° power splitter. One output was fed back to the lock-in amplifier where the resonant frequency and amplitude can be tracked. By controlling the operating phase, stable operation beyond the critical bifurcation regime can be obtained [6]. The other output signal, after additional amplification, was fed into an AlazarDSO ATS9360 digitizer for ringdown capturing (sampling rate set to  $\sim 10\times$  device's natural frequency). A voltage-controlled RF switch, placed between the lock-in output and the resonator, acts as the mechanism for cutting the excitation. When the trigger voltage is set 'high', the connection between the lock-in and resonator is closed, therefore stable oscillatory signal can be recorded by the AlazarDSO. When the trigger voltage is switched to 'low', the falling edge cuts the input to the resonator and triggers the digitizer, and thus the full ringdown response can be captured. Lastly, the resonator displacement can be estimated from the measured output voltage ( $V_{out}$ ) using the total trans-impedance gain  $G_{tot}$  of the amplifiers as

$$a \cong \frac{V_{out}d_0^2}{2\pi f_0 G_{tot} V_b \epsilon_0 A}. \quad (12)$$

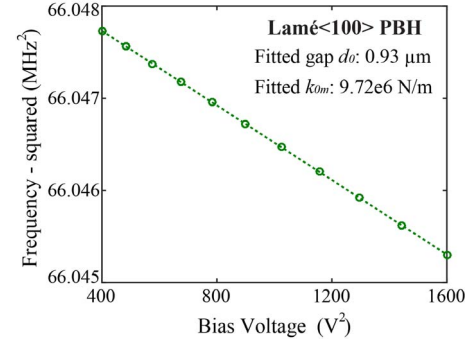


Fig. 6. Example of electrostatic frequency tuning result for Lamé (100) under PBH doping, where the markers denote the measured data and the line is the fitted using (13). This allows estimation of  $k_{0m}$  and  $d_0$ .

It is worth mentioning that even under linear vibrations, higher order harmonics can be generated due to the inverse relationship between output current and resonator displacement. However, the contributions of higher order harmonics are small as compared with the main harmonic if  $a \ll d_0$ . Therefore it is valid to use (12) as a first order approximation.

## V. EXPERIMENTAL RESULTS

Three type of experiments were carried out to characterize the resonator nonlinear behavior: electrostatic frequency tuning, closed-loop frequency response, and ringdown measurements.

### A. Electrostatic Frequency Tuning

As seen in the previous analysis, it is critical to know the actual gap size ( $d_0$ ) and linear spring constant ( $k_{0m}$ ) in order to estimate parameters such as resonator displacement (12), the electrostatic spring constants (8), and the  $A$ - $f$  coefficient (2) & (3) etc. However, due to fabrication tolerances (e.g. lateral over-etching), the actual gap size may vary from the designed layout. Previous research also show that  $k_{0m}$  varies under different doping type/levels. Therefore it would be desirable if these resonator properties are known beforehand.

From (9) we see that the linear resonant frequency decreases as the bias voltage increases, this can be used as a method of extracting device properties. It should be noted that there are three unknowns in (9):  $m$ ,  $d_0$ , and  $k_{0m}$ . In this study, we chose to extract  $k_{0m}$  and  $d_0$  by substituting the simulated  $m$  and fitting  $f_0^2$  vs.  $V_b^2$  using

$$m(2\pi f_0)^2 = k_{0m} - \frac{1}{d_0^3} N A \epsilon_0 V_b^2. \quad (13)$$

As seen in Fig. 6,  $k_{0m}$  can be extracted from the y-intercept and  $1/d_0^3$  can be extracted from the slope. The extracted  $k_{0m}$  and  $d_0$  are listed in [30], where the difference between measured and simulated  $k_{0m}$  are within 5%.

### B. Closed-Loop Frequency Response

Shown in Fig. 7 are the closed-loop frequency response for various resonators, where the ac excitation voltage is gradually increased to drive the device from the linear to the nonlinear operating regime. From these measurements,  $\kappa$  can

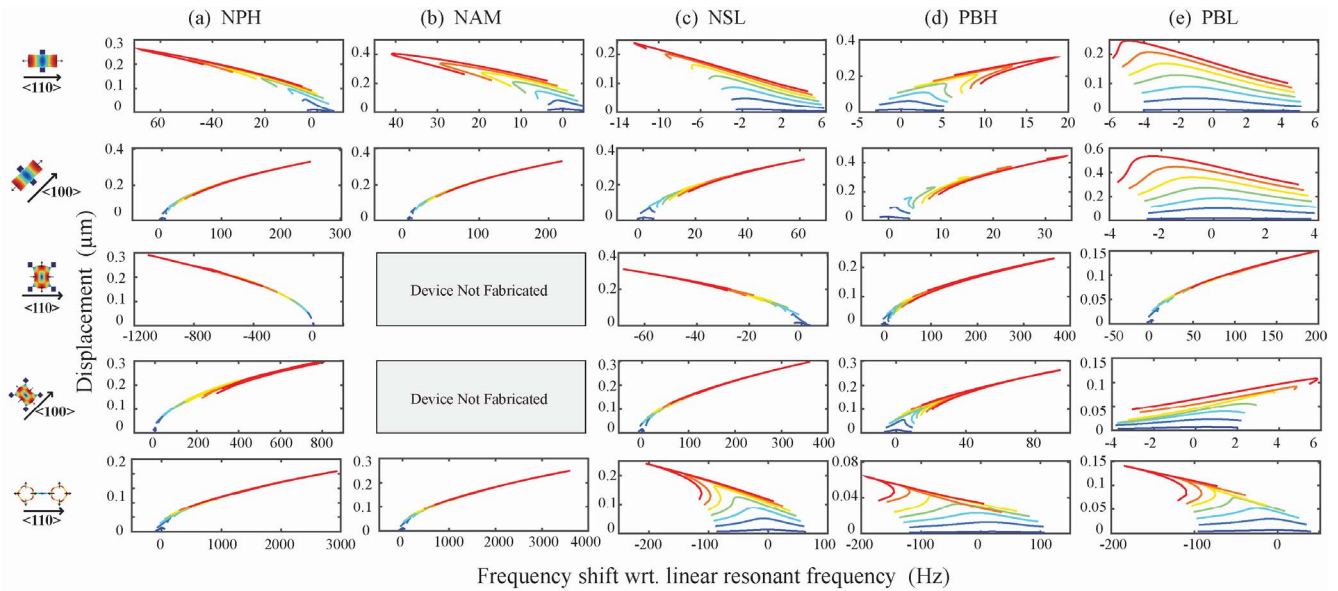


Fig. 7. Closed-loop frequency response for three families of resonators. The x-axis plots  $f - f_0$  in 'Hz' and the y-axis plots resonator displacement in ' $\mu\text{m}$ '. Each row represents a family of resonators of the same mode shape and with a particular crystal orientation, and each column represents a similar doping level. For each family of devices, the same operating conditions are maintained. The ac excitation voltage was gradually increased from low (blue-colored curves) to high (red-colored curves) to drive the resonators into nonlinear oscillation regime. To ensure valid comparison, the electrical feedthrough effects have also been subtracted. For wafer labeling, see Table II notes.

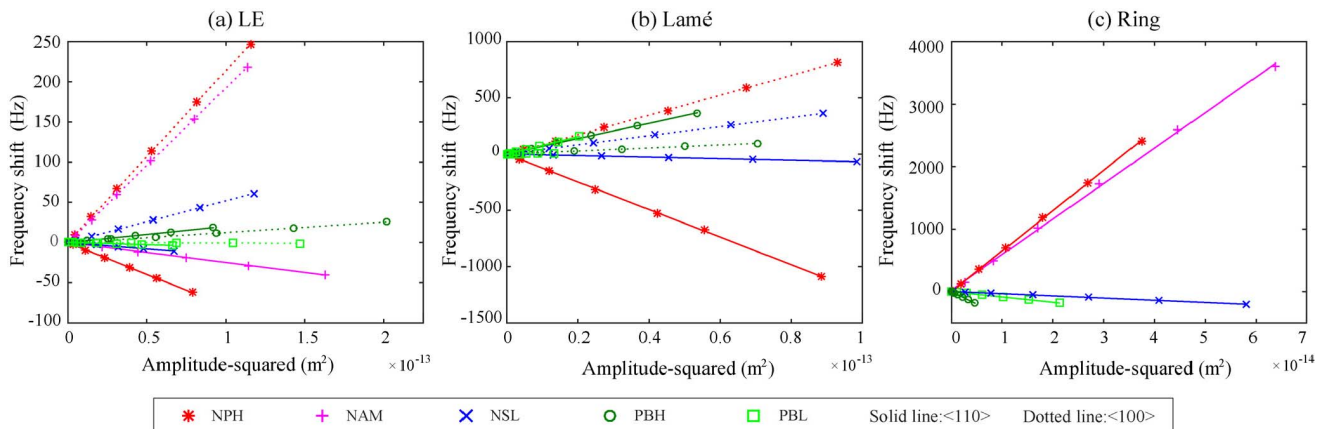


Fig. 8. Fitted  $\kappa$  from the closed-loop frequency response for (a) LE, (b) Lamé, and (c) Ring resonators. The markers indicates the measurement results, the lines are fitted results, and the slope represents  $\kappa$ . For each family of devices, the bias voltage was held constant for valid comparison (LE: 25V, Lamé: 30V, Ring: 20V). For wafer labeling, see Table II notes.

be extracted by tracking the maximum vibrational amplitude and its corresponding frequency shift with respect to the linear resonant frequency, and fitting the results using (2). Figure 8 plots the frequency shift versus the modal amplitude-squared for all devices, where the slopes of the linear fitted lines represent  $\kappa$ .

### C. Ringdown Measurements

The ringdown response of the  $\langle 110 \rangle$  oriented Ring resonator under Phosphorous doping, tested at  $0^\circ\text{C}$  temperature and 25 V bias voltage, is used below as a demonstration of the analysis procedure. First, the ringdown response is captured with a fixed bias voltage and different initial ac excitation voltages. Using the FFT method detailed in §II-B with a bin size of 16000, the frequency and amplitude information

as a function of time can be tracked (Fig. 9a and 9b). Figure 9c plots the extracted amplitude with respect to time, and from this the resonator  $Q$  can be extracted ( $\sim 257.3k$ ). The frequency during the ringdown period is plotted in Fig. 9d. When the ac excitation is small, no obvious frequency shift is observed during the ringdown (blue curve in Fig. 9d), and as the ac excitation increases, the frequency shift becomes more pronounced. Using the extracted information, the frequency-amplitude relation can be obtained. From Fig. 9e it is clear that the ringdown frequency follows the same backbone curve for the different driving amplitudes used to excite initial oscillations, and provides another pathway for estimating  $\kappa$ . The  $A$ - $f$  coefficients for the various devices under study can be extracted using the method detailed above, with the results plotted in Fig. 10.



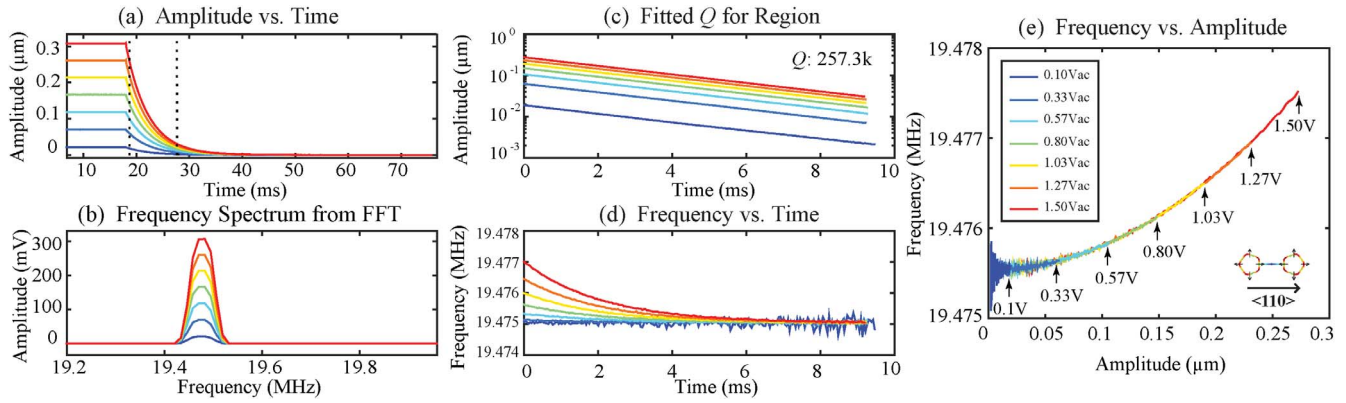


Fig. 9. Process of extracting  $\kappa$  using the ringdown method for the highly phosphorus-doped,  $\langle 110 \rangle$  aligned Ring resonator. (a) Ringdown envelope for device tested under fixed  $V_b$  and increasing  $V_{ac}$ , where the region between the vertical dotted lines is divided into bins of 16000 for data extraction. (b) Typical FFT response of one bin. (c) Amplitude vs. time for the entire ringdown curve. (d) Interpolated frequency vs. time for the entire ringdown curve. (e) Frequency vs. amplitude as the device rings-down. The color coding in (e) applies to all subplots.

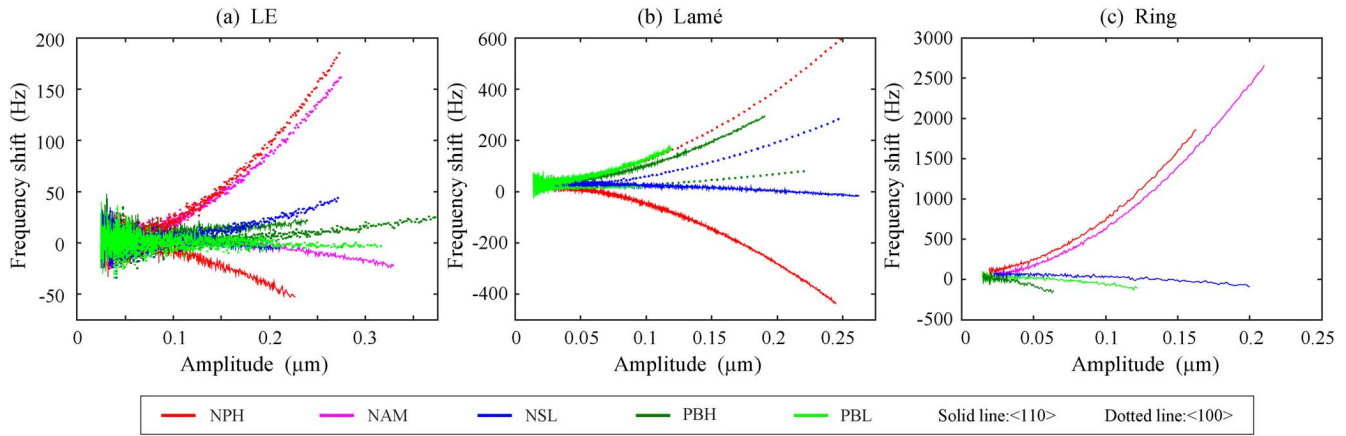


Fig. 10. Extracted frequency-amplitude relationship for (a) LE, (b) Lamé, and (c) Ring resonators using the ringdown method. For each family of devices, the bias voltage was held constant for valid comparison (LE: 25V, Lamé: 30V, Ring: 20V). For wafer labeling, see Table II notes.

#### D. Summary of Doping Affecting Resonator Nonlinearity

Based on the results of both the closed-loop frequency response and ringdown response, a few observations can be made:

- The sign change of  $\kappa$  for most devices indicates that material nonlinearity is the dominant factor, as both geometrical and electrostatic nonlinearities would not result in a sign change in nonlinear behavior.
- For any particular type of resonator oriented along the same crystalline direction, the nonlinear behavior varies dramatically as doping changes. For example, the Ring resonator shows a hardening effect for Phosphorus (NPH) and Arsenic (NAM) doping, whereas for Antimony (NSL) and Boron (PBH and PBL) doping, the resonator shows a softening effect.
- For any particular type of resonator under the same doping condition, the nonlinearity may be affected by device orientation. For example, the LE resonator under Phosphorus doping shows a softening response for the  $\langle 110 \rangle$  orientation and a hardening response for  $\langle 100 \rangle$  direction.
- The doping concentration also affects the nonlinear behavior. For nearly all resonators tested, a trend of

$$|\kappa_{NPH}| > |\kappa_{NAM}| > |\kappa_{NSL}| \text{ for n-type doping, and } |\kappa_{PBH}| > |\kappa_{PBL}| \text{ for p-type doping can be observed.}$$

#### E. Effect of Bias Voltage on Measured A-f Coefficient

To analyze the effect of bias voltage on  $\kappa$ , each family of devices were tested under different bias voltages using measurements of forced oscillation and ringdown. Taking into consideration that too small of a voltage would decrease the signal-to-noise ratio, and too large of a voltage would cause permanent device failure such as electrical shorting, the devices were only tested within a certain voltage span (LE: 25V - 35V, Lamé: 30V- 40V, Ring: 20V- 30V).

Figure 11 plots the measured  $\kappa$  using both closed-loop amplitude-frequency and ringdown methods under different bias voltages, and no clear trend of bias voltage dependency on  $\kappa$  can be observed. This suggests that the effect of electrostatic nonlinearities are small in comparison with mechanical nonlinearities. One can also estimate the contribution of electrostatic nonlinearities towards  $\kappa$  by substituting (8) into (3), which for the various types of resonators in this work, the electrostatic contribution is orders-of-magnitude smaller than that of the mechanical contribution. This result is similar

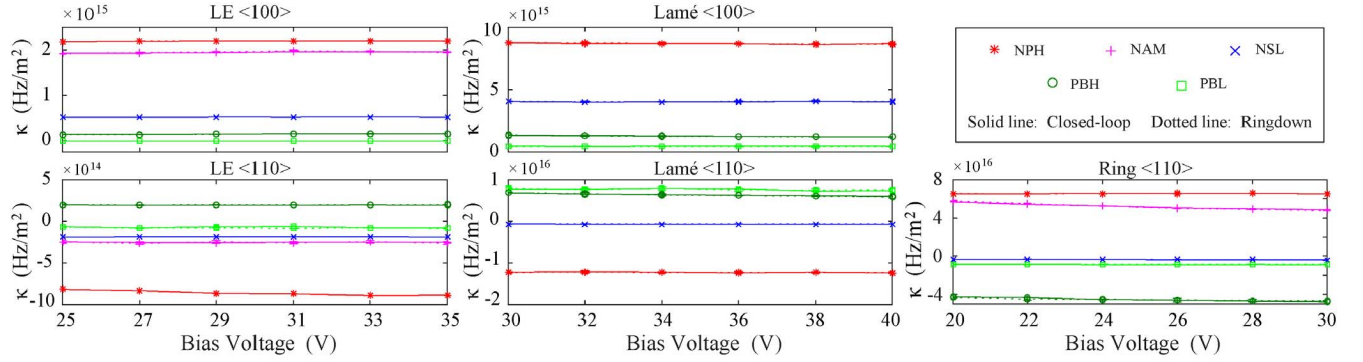


Fig. 11. Comparison of the  $A$ - $f$  coefficient  $\kappa$  from both closed-loop frequency response and ringdown analysis under different bias voltages. The solid lines represent closed-loop, while the dotted lines represent ringdown. The error associated with each device is estimated based on §V-B. The overlapping of the two lines indicate that the results obtained using the two methods are almost identical. The nearly horizontal lines also indicate that  $\kappa$  has minimal bias voltage dependency, and hence the dominant factor is material nonlinearity.

to the observations made in [14], [15], and [21], where the resonator nonlinear behavior was dominated by mechanical nonlinearities rather than electrostatic ones.

## VI. DISCUSSION

### A. Comparison Between Frequency Response and Ringdown

The  $A$ - $f$  coefficients obtained from spectral and time-domain methods are compared in Fig. 11. Relative variation between the spectral and time-domain methods is  $<4\%$ , which lies within the measurement error. This fact proves the validity of both methods for characterization of the nonlinear stiffness in MEMS resonators. Discrepancies between the two methods may arise from certain aspects such as the estimation of the effective trans-impedance gain to both the lock-in amplifier and digitizer for devices at various frequencies (see  $G_1$  and  $G_2$  in Fig. 5). Other error sources may arise from the difference between the lock-in amplifier and digitizer's internal 10MHz clock references, which will affect the absolute frequency measurement.

Comparing the two measurement techniques, there exist pros and cons for each method. For the ringdown method, the experimental setup and post data analysis can be more complicated than the closed-loop frequency response. However, the ringdown response may also provide benefits such as eliminating effect of feedthrough (i.e. no  $V_{ac}$  excitation during the ringdown), as well as being able to analyze other dynamical effects such as nonlinear damping etc. [9].

### B. Result Accuracy: Uncertainty Analysis

The accuracy of  $\kappa$  can be estimated by performing an uncertainty propagation analysis from (2) as

$$\frac{\delta_\kappa}{\kappa} = \sqrt{\left(\frac{\delta_{\Delta f}}{\Delta f}\right)^2 + \left(2\frac{\delta_a}{a}\right)^2}, \quad (14)$$

where  $\delta$  is the uncertainty associated with each terms. The uncertainty of  $a$  can be estimated from (12) as

$$\left(\frac{\delta_a}{a}\right)^2 \cong \left(\frac{\delta V_{out}}{V_{out}}\right)^2 + \left(2\frac{\delta d_0}{d_0}\right)^2 + \left(\frac{\delta f_0}{f_0}\right)^2 + \left(\frac{\delta G_{tot}}{G_{tot}}\right)^2. \quad (15)$$

Equations (14) and (15) includes the possible factors that may introduce error, and they are analyzed individually:

- Gap size estimation ( $\delta_{d_0}/d_0$ ): based on (14) and (15), error in  $d_0$  has the largest contribution towards the total error. Even though electrostatic frequency tuning was used to facilitate estimation of the actual gap size (see §V-A), errors that arise from fabrication uncertainties such as trench tapering and lateral etch uniformity cannot be captured. Based on SEM measurements, the gap size typically varies by about  $\pm 0.1 \mu\text{m}$  across the wafer and across the trench profile, and for a typical  $1 \mu\text{m}$  gap, this leads to  $\delta_{d_0}/d_0 = 10\%$ .
- Frequency uncertainty ( $\delta_{\Delta f}/\Delta f$  and  $\delta_{f_0}/f_0$ ): we believe that the uncertainty in the frequency measurement mainly arises from temperature-induced frequency shifts, which is also device and doping dependent [17]. For ringdown measurements, the temperature change is negligible, as the ringdown time constants are on the order of tens of milliseconds. However, for closed-loop frequency sweeps that are taken over a few minutes, the environmental chamber used for temperature control was observed to have fluctuation of  $\pm 0.02^\circ\text{C}$  at  $0^\circ\text{C}$ . For devices used in this study, the temperature coefficient of frequency ranges from  $-30$  to  $15 \text{ ppm}/^\circ\text{C}$ , this leads to frequency accuracy of  $\pm 0.6 \text{ ppm}$ . While this frequency shift may be considerably small for  $\delta_{f_0}/f_0$ , the uncertainty is much larger for  $\delta_{\Delta f}/\Delta f$  as  $\Delta f$  is also at the ppm level.
- Voltage error ( $\delta_{V_{out}}/V_{out}$ ): voltage noise may be introduced from the lock-in amplifier, the TIA, and the digitizer input. Based on the measurement result, the voltage noise is within  $\pm 1 \text{ mV}$  range, which leads to a maximum  $\delta_{V_{out}}/V_{out}$  within  $\pm 10\%$ . This worst case scenario is estimated based on the case when the resonator amplitude is the smallest ( $V_{out} \cong 10 \text{ mV}$ ). As amplitude increases,  $\delta_{V_{out}}/V_{out}$  decreases accordingly.
- TIA gain estimation ( $\delta_{G_{tot}}/G_{tot}$ ):  $G_{tot}$  used in this study is characterized by inputting a known current source and measuring the output voltage, therefore we believe that  $\delta_{G_{tot}}/G_{tot}$  should be  $< 5\%$ , which mostly arise from non-uniform gain across frequency.



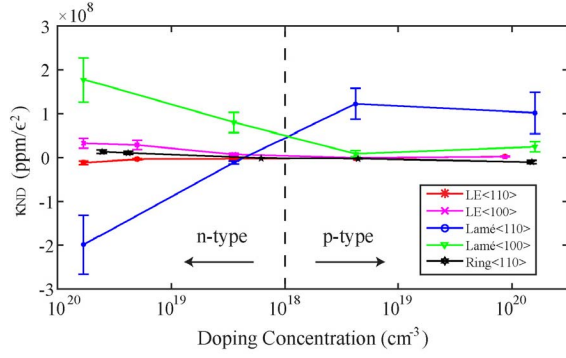

 Fig. 12.  $\kappa_{ND}$  vs. doping for all devices tested.  $\kappa_{dim}$  is calculated using (16).

 TABLE III  
 COMPARISON OF  $\kappa$  FOR LE RESONATOR UNDER NAM DOPING

Wafer	Dopant	Resistivity, m $\Omega$ -cm	Concentration, cm <sup>-3</sup>
PBH	Boron	1.4	8.7e+19
		Lamé: 0.8 Ring: 0.9	Lamé: 1.6e+20 Ring: 1.5e+20
PBL	Boron	16.4, Ring: 15.9	4.2e+18 Ring: 4.4e+18
NPH	Phosphorous	1.3 Ring: 1.8	5.9e+19 Ring: 4.1e+19
NAM	Arsenic	3.5 Ring: 3.1	2.0e+19 Ring: 2.4e+19
NSL	Antimony	11.7	2.8e+18
		Ring: 17.1	Ring: 1.6e+18

\* The resistivities and concentrations are the same for all devices unless noted otherwise. The wafer labeling follows the logic: doping type, dopant, and level of doping (H: high; M: medium; L: low).

### C. Result Utilization

The  $\kappa$  values reported above are associated only with the particular resonator geometry (frequency/dimension); scaling these resonators results in varying  $\kappa$ . To extend these results to predict the nonlinearity of devices with similar mode shapes,  $\kappa$  can be expressed as a non-dimensionalized parameter (unit: ppm/ $\epsilon^2$ )

$$\kappa_{ND} = \frac{10^6 \Delta f / f_0}{(a/L_{eff})^2}, \quad (16)$$

where  $L_{eff}$  can be substituted by half beam length, full plate length, and average radius for the LE, Lamé, and Ring resonator respectively. Intuitively,  $\kappa_{ND}$  relates the frequency shift to the strain within the system. This also assumes that the electrostatic and geometric nonlinearities can be neglected, and  $\kappa$  is dominated by material nonlinearity as shown above. Based on the above analysis, the uncertainty associated with each device is plotted as error bars in Fig. 12. The error varies depending on device geometry and doping, but is typically around  $\pm 40\%$ .

A typical use of these  $\kappa_{ND}$  numbers is to predict the nonlinearity of resonators of a given doping and for the common mode shapes in this work. Table III illustrates  $\kappa$  values from two LE resonators of similar doping but with different geometries. The resonant frequencies and lengths are different

but both yield a similar  $\kappa_{ND}$ . The resulting discrepancy is within the experimental error bounds, and could also be in part due to the mode shape of the two resonators being slightly different. The data presented in Fig. 12 can thus be used for obtaining a general sense of the nonlinearity when designing resonators in doped silicon.

## VII. CONCLUSION

This paper examines the nonlinear behavior of bulk-mode silicon MEMS resonators under degenerate doping. Two ways of analyzing the nonlinear system: amplitude-frequency response and ringdown analysis, are demonstrated both analytically and experimentally. The experimental results obtained from both methods are within 4% variation, and suggest that in comparison with electrical nonlinearities, mechanical nonlinearities play a dominant role in the systems' nonlinear behavior. Experimental results also show that by changing the doping and/or orientation, either softening or hardening nonlinear behavior can be observed for the same design. This indicates that both doping and crystal orientation will affect the systems' nonlinear behavior, and that one can manipulate these nonlinear effects, and even minimize them, by choosing the correct doping and orientation, thereby providing a means of extending the linear dynamic range of the device.

Overall, because of the strength and complexity of the nonlinearities depend on the level of doping and the device orientation, it is important for designers to understand and anticipate these nonlinearities in their devices. In addition, these observations suggest research into the fundamental causes of these effects, with the goal of developing predictive models so that a priori design of nonlinearity can be realized.

## APPENDIX

List of nonlinear equation of motion developed for commonly used bulk-mode resonators (ignore damping):

- LE (referenced from [13]):

$$\frac{\rho A L_0}{2} \frac{\partial^2 x}{\partial t^2} = -\frac{\pi^2}{4} \left( \frac{2E_0 A}{L_0} x + \frac{16E_1 A}{3L_0^2} x^2 + \frac{3\pi^2 E_2 A}{2L_0^3} x^3 \right). \quad (a-1)$$

- Lamé (referenced from [15]):

$$\frac{\rho A L_0}{2} \frac{\partial^2 x}{\partial t^2} = -\pi^2 G_0 h x + \frac{128\pi G_1 h}{9L_0} x^2 - \frac{9\pi^4 G_2 h}{4L_0^2} x^3. \quad (a-2)$$

where  $\gamma$  is the shear strain and  $G = G_0 + G_1\gamma + G_2\gamma^2$  is the strain dependent shear modulus.

- Ring (referenced from [21]):

$$\rho A_0 \frac{\partial^2 u_r}{\partial t^2} = \frac{\partial}{\partial r} \left[ \frac{EA}{1-\nu^2} \left( \frac{\partial u_r}{\partial r} + \nu \frac{u_r}{r} \right) \right] + \frac{EA_0}{r(1+\nu)} \left( \frac{\partial u_r}{\partial r} + \frac{u_r}{r} \right), \quad (a-3)$$

$$A = A_0(1 - \nu \partial u_r / \partial r)$$

and

$$E = E_0 + E_2(\partial u_r / \partial r)^2.$$

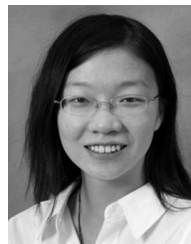
where  $u_r$  is the radial displacement,  $\nu$  is the Poisson's ratio,  $A_0$  and  $A$  is the initial and actual transduction area.

#### ACKNOWLEDGMENT

The authors would like to thank the staffs at Stanford Nanofabrication Facility, staffs at Lurie Nanofabrication Facility, and Gary Yama from Bosch Research and Technology Center for their help during the fabrication process.

#### REFERENCES

- [1] C. T.-C. Nguyen, "Frequency-selective MEMS for miniaturized low-power communication devices," *IEEE Trans. Microw. Theory Techn.*, vol. 47, no. 8, pp. 1486–1503, Aug. 1999.
- [2] J. T. M. van Beek and R. Puers, "A review of MEMS oscillators for frequency reference and timing applications," *J. Micromech. Microeng.*, vol. 22, no. 1, p. 013001, 2012.
- [3] R. Melamud *et al.*, "MEMS enables oscillators with sub-ppm frequency stability and sub-ps jitter," in *Proc. Solid-State Sensors, Actuators, Microsyst. Workshop*, Hilton Head, SC, USA, 2012, pp. 66–69.
- [4] S. S. Nasiri and A. F. Flannery, "Vertically integrated MEMS structure with electronics in a hermetically sealed cavity," U.S. Patent 7104129 B2, Sep. 12, 2006.
- [5] T. Mattila *et al.*, "A 12 MHz micromechanical bulk acoustic mode oscillator," *Sens. Actuators A, Phys.*, vol. 101, pp. 1–9, Sep. 2002.
- [6] H. K. Lee, R. Melamud, S. Chandorkar, J. Salvia, S. Yoneoka, and T. W. Kenny, "Stable operation of MEMS oscillators far above the critical vibration amplitude in the nonlinear regime," *J. Microelectromech. Syst.*, vol. 20, no. 6, pp. 1228–1230, 2011.
- [7] V. Kaajakari, T. Mattila, A. Oja, and H. Seppa, "Nonlinear limits for single-crystal silicon microresonators," *J. Microelectromech. Syst.*, vol. 13, no. 5, pp. 715–724, Oct. 2004.
- [8] S. Zaitsev, O. Shtempluck, E. Buks, and O. Gottlieb, "Nonlinear damping in a micromechanical oscillator," *Nonlinear Dyn.*, vol. 67, no. 1, pp. 859–883, 2012.
- [9] P. M. Polunin, Y. Yang, M. I. Dykman, T. W. Kenny, and S. W. Shaw, "Characterization of MEMS resonator nonlinearities using the ringdown response," *J. Microelectromech. Syst.*, vol. 25, no. 2, pp. 297–303, Apr. 2016.
- [10] A. Barari, H. D. Kaliji, M. Ghadimi, and G. Domairry, "Non-linear vibration of Euler–Bernoulli beams," *Latin Amer. J. Solids Struct.*, vol. 8, no. 2, pp. 139–148, 2011.
- [11] D. H. Hodges, R. A. Ormiston, and D. A. Peters, "On the nonlinear deformation geometry of Euler–Bernoulli beams," NASA AVRADCOM Tech. Rep. 80-A-1, Apr. 1980.
- [12] M. Agarwal *et al.*, "Nonlinear characterization of electrostatic MEMS resonators," in *Proc. IEEE Int. Freq. Control Symp. Expo.*, Jun. 2006, pp. 209–212.
- [13] V. Kaajakari, T. Mattila, A. Lipsanen, and A. Oja, "Nonlinear mechanical effects in silicon longitudinal mode beam resonators," *Sens. Actuators A, Phys.*, vol. 120, no. 1, pp. 64–70, 2005.
- [14] L. C. Shao, M. Palaniapan, L. Khine, and W. W. Tan, "Nonlinear behavior of Lamé-mode SOI bulk resonator," in *Proc. IEEE Int. Freq. Control Symp.*, May 2008, pp. 646–650.
- [15] H. Zhu, G. C. Shan, C. H. Shek, and J. E.-Y. Lee, "Shear dependent nonlinear vibration in a high quality factor single crystal silicon micromechanical resonator," *Appl. Phys. Lett.*, vol. 101, no. 3, p. 034102, 2012.
- [16] A. K. Samarao and F. Ayazi, "Temperature compensation of silicon micromechanical resonators via degenerate doping," in *Proc. IEEE Int. Electron Devices Meeting*, Dec. 2009, pp. 1–4.
- [17] E. J. Ng, V. A. Hong, Y. Yang, C. H. Ahn, C. L. M. Everhart, and T. W. Kenny, "Temperature dependence of the elastic constants of doped silicon," *J. Microelectromech. Syst.*, vol. 25, no. 3, pp. 730–741, Jun. 2015.
- [18] T. Pensala, A. Jaakkola, M. Prunnila, and J. Dekker, "Temperature compensation of silicon MEMS resonators by heavy doping," in *Proc. IEEE Int. Ultrason. Symp.*, Oct. 2011, pp. 1952–1955.
- [19] J. J. Hall, "Electronic effects in the elastic constants of *n*-type silicon," *Phys. Rev.*, vol. 161, pp. 756–761, Sep. 1967.
- [20] R. W. Keyes, "Electronic effects in the elastic properties of semiconductors," *Solid State Phys.*, vol. 20, pp. 37–90, Dec. 1968.
- [21] S. Wang *et al.*, "Nonlinearity of hermetically encapsulated high- $Q$  double balanced breathe-mode ring resonator," in *Proc. IEEE 23rd Int. Conf. Micro Electro Mech. Syst. (MEMS)*, Jan. 2010, pp. 715–718.
- [22] A. Bijari, S. H. Keshmiri, and W. Wanburee, "Nonlinear modeling and investigating the nonlinear effects on frequency response of silicon bulk-mode ring resonator," *Iranian J. Electr. Electron. Eng.*, vol. 8, no. 1, pp. 45–54, 2012.
- [23] M. Shahmohammadi, H. Fatemi, and R. Abdolvand, "Nonlinearity reduction in silicon resonators by doping and re-orientation," in *Proc. IEEE Int. Conf. Micro Electro Mech. Syst. (MEMS)*, Jan. 2013, pp. 793–796.
- [24] Y. Yang *et al.*, "Measurement of the nonlinear elasticity of doped bulk-mode MEMS resonators," in *Proc. Solid-State Sensors, Actuators, Microsyst. Workshop*, Hilton Head, SC, USA, 2014, pp. 8–12.
- [25] R. Lifshitz and M. C. Cross, "Nonlinear dynamics of nanomechanical and micromechanical resonators," in *Reviews of Nonlinear Dynamics and Complexity*. Hoboken, NJ, USA: Wiley, 2008, pp. 1–52.
- [26] L. D. Landau and E. M. Lifshitz, *Mechanics*. Oxford, U.K.: Butterworth, 1976.
- [27] A. H. Nayfeh and D. T. Mook, *Nonlinear Oscillations*. New York, NY, USA: Wiley, 2007.
- [28] H. Lee, "Frequency stability of micromechanical oscillators with nonlinearities," Ph.D. dissertation, Dept. Mech. Eng., Stanford Univ., Stanford, CA, USA, 2011.
- [29] R. N. Candler *et al.*, "Long-term and accelerated life testing of a novel single-wafer vacuum encapsulation for MEMS resonators," *J. Microelectromech. Syst.*, vol. 15, no. 6, pp. 1446–1456, Dec. 2006.
- [30] Y. Yang, "Nonlinearities of bulk acoustic mode silicon micromechanical resonators," Ph.D. dissertation, Dept. Mech. Eng., Stanford Univ., Stanford, CA, USA, 2016.
- [31] A. Partridge and M. Lutz, "Episeal pressure sensor and method for making an episeal pressure sensor," U.S. Patent 6928879, Aug. 16, 2005.
- [32] E. J. Ng, Y. Yang, Y. Chen, and T. W. Kenny, "An etch hole-free process for temperature-compensated, high  $Q$ , encapsulated resonators," in *Proc. Solid-State Sensors, Actuators, Microsyst. Workshop*, Hilton Head, SC, USA, Jun. 2014, pp. 99–100.
- [33] C. Tu and J. E.-Y. Lee, "Study on thermoelastic dissipation in bulk mode resonators with etch holes," in *Proc. 7th IEEE Int. Conf. Nano/Micro Eng. Molecular Syst. (NEMS)*, Mar. 2012, pp. 478–482.
- [34] Y. Yang, E. J. Ng, Y. Chen, I. B. Flader, and T. W. Kenny, "A unified epi-seal process for fabrication of high-stability microelectromechanical devices," *J. Microelectromech. Syst.*, vol. 25, no. 3, pp. 489–497, Jun. 2016.
- [35] EL-CAT. INC. *Properties of Silicon and Silicon Wafers: Resistivity & Mobility Calculator*, accessed on Oct. 2015. [Online]. Available: <https://www.el-cat.com/silicon-properties.html>



**Yushi Yang** received the bachelor's degrees from Purdue University and Shanghai Jiao Tong University in 2011, and the M.S. and Ph.D. degree from Stanford University in 2013 and 2016, respectively, all in mechanical engineering. Her research interests include developing MEMS fabrication techniques, studying the nonlinear behavior of bulk-mode MEMS resonators, and analyzing the coupling behavior of MEMS resonators.



**Eldwin J. Ng** received the B.S. degree from the University of California, Berkeley in 2009, and the M.S. and Ph.D. degrees from Stanford University in 2012 and 2015, respectively, all in mechanical engineering. He is currently with InvenSense Inc. His research interests include microfabrication technologies, RF resonators, and MEMS sensors. He received the B.S. and Ph.D. scholarship from the Agency for Science, Technology and Research, Singapore.



**Pavel M. Polunin** received the B.S. degree in automation from Bauman Moscow State Technical University, Moscow, Russia, in 2009, and the M.S. degree in mechanical engineering from Michigan State University, East Lansing, MI, USA, in 2013, where he is currently pursuing the Ph.D. degree with the Department of Mechanical Engineering, and the Department of Physics and Astronomy. His research interests include nonlinear dynamics of MEMS resonators and sensors, noisy systems, reduced order analysis, system modeling, and parameter characterization from design and experiments.



**Yunhan Chen** received the B.S. degree in mechanical engineering from Tsinghua University, Beijing, China, in 2011, and the M.S. degree in mechanical engineering from Stanford University, Stanford, CA, USA, in 2013, where he is currently pursuing the Ph.D. degree under the Stanford Graduate Fellowship. His research interests include microfabrication technologies, ovenized MEMS resonators, and MEMS sensors.



**Ian B. Flader** received the B.S. (*summa cum laude*) degree in mechanical engineering from the University of Tennessee, Knoxville, in 2012, and the M.S. degree in mechanical engineering from Stanford University in 2016, where he is currently pursuing the Ph.D. degree. His research interests include disk resonating gyroscopes, modal coupling, nonlinearities in resonant structures, topological and gradient-free optimization, and automatic control.



**Steven W. Shaw** received the B.A. degree in physics from the University of Michigan-Flint in 1978, the M.S.E. degree in applied mechanics from the University of Michigan-Ann Arbor in 1979, and the Ph.D. degree in theoretical and applied mechanics from Cornell in 1983. He is currently a Harris Professor of Mechanical and Aerospace Engineering with the Florida Institute of Technology in Melbourne, Florida, and a University Distinguished Professor with the Department of Mechanical Engineering and an Adjunct Professor with the Department of Physics and Astronomy, Michigan State University in East Lansing, Michigan.

He held visiting appointments with Cornell University, University of Michigan, Caltech, University of Minnesota, University of California-Santa Barbara, and McGill University. He currently an Associate Editor for two journals, nonlinear dynamics, and the *SIAM Journal on Applied Dynamical Systems*. His research interests are in applied dynamical systems and currently include modeling, analysis, and design of micro-scale resonators for sensing and signal processing applications and nonlinear vibration absorbers for automotive applications.

Dr. Shaw is a member and fellow of the ASME and a recipient of the SAE Arch T. Colwell Merit Award, the Henry Ford Customer Satisfaction Award, the ASME Henry Hess Award, and the ASME N. O. Myklestad Award.



**Mark I. Dykman** received the M.S. degree from Kiev State University in 1972, the Ph.D. degree from the Institute of Metal Physics, Ukrainian Academy of Science, in 1973, and the Ph.D. degree from the Institute of Semiconductors, Ukrainian Academy of Science, in 1984, all in physics. He was with the Institute of Semiconductors, Kiev, from 1972 to 1991, and Stanford University from 1992 to 1994. He has been with Michigan State University since 1995. He held visiting appointments a Professor of Physics with Lancaster University, U.K., an EPSRC Visiting Research Fellow, U.K., and a Visiting Scholar with the NASA Exploration Systems Directorate. He is currently a Professor of Physics with Michigan State University. His major areas of interest include condensed matter physics, nonlinear dynamics, transport phenomena, statistical physics far from thermal equilibrium, and quantum computing. He serves on the Editorial Board of *Fluctuations and Noise Letters*. He is a Fellow of the American Physical Society.



**Thomas W. Kenny** received the B.S. degree in physics from the University of Minnesota, Minneapolis, in 1983, and the M.S. and Ph.D. degrees in physics from the University of California, Berkeley, in 1987 and 1989, respectively. From 1989 to 1993, he was with the Jet Propulsion Laboratory, National Aeronautics and Space Administration, Pasadena, CA, USA, where his research focused on the development of electron-tunneling high-resolution microsensors. In 1994, he joined the Department of Mechanical

Engineering, Stanford University, Stanford, CA, where he directs microsensor-based research in a variety of areas, including resonators, wafer-scale packaging, cantilever beam force sensors, microfluidics, and novel fabrication techniques for micromechanical structures. He is the Founder and the CTO of Cooligy (now a division of Emerson), a microfluidics chip cooling component manufacturer, and the Founder and a Board Member of SiTime Corporation (now a division of MegaChips), a Developer of timing references using MEMS resonators. He is the Founder and a Board Member of Applaud Medical, developing non-invasive therapies for kidney stones. He is currently the Richard Weiland Professor of Mechanical Engineering and the Senior Associate Dean of Engineering for Student Affairs. He was the General Chairman of the 2006 Hilton Head Solid State Sensor, Actuator, and Microsystems Workshop, and the General Chair of the Transducers 2015 meeting in Anchorage. From 2006 to 2010, he was on leave to serve as a Program Manager with the Microsystems Technology Office, the Defense Advanced Research Projects Agency, starting and managing programs in thermal management, nano-manufacturing, manipulation of Casimir forces, and the Young Faculty Award. He has authored or coauthored over 250 scientific papers and is a holder of 50 issued patents, and has been advisor to over 50 graduated Ph.D. students from Stanford.